remote sensing

Article

Improved Main Lobe Cancellation Method for Suppression Directional Noise in HFSWR Systems

Dezhu Xiao , Xin Zhang , Qiang Yang * and Jiaming Li

School of Electronics and Information Engineering, Harbin Institute of Technology, Harbin 150001, China; 21b905050@stu.hit.edu.cn (D.X.); zhangxinhit@hit.edu.cn (X.Z.); 18b905030@stu.hit.edu.cn (J.L.)
* Correspondence: yq@hit.edu.cn; Tel.: +86-136-1363-9936

Abstract: High frequency surface wave radar (HFSWR) has been successfully developed for early warning, especially for vessel target detection. However, the system's performance is consistently constrained by external environmental noise, particularly directional noise, which presents a new problem for HFSWR. Anisotropic directional noise has complex behavior, and its noise level is generally increased by 10 to 15 dB compared to traditional noise floor level. Suppressing varying directional noise and exploring obscured targets are challenging tasks for HFSWR. In this paper, a novel algorithm based on angle-Doppler joint multi-eigenvector synthesis, which considers the angle-Doppler map of radar echoes, is adopted to analyze the characteristics of the directional noise. Given the measured data set, we first analyze the directional noise-spatial correlation. Then, an algorithm based on sliding main lobe cancellation (SL-MLC) based on a sliding single-notch space filter (SSNSF) is proposed to block target components and get training data that contains precise directional noise information. Finally, the method is examined by measured data, and the results indicate the method has better performance for directional noise than the compared method.

Keywords: high frequency surface radar (HFSWR); directional noise; main lobe cancellation; correlation analysis; target detection

Citation: Xiao, D.; Zhang, X.; Yang, Q.; Li, J. Improved Main Lobe Cancellation Method for Suppression Directional Noise in HFSWR Systems. *Remote Sens.* **2024**, *16*, 254. https://doi.org/10.3390/rs16020254

Academic Editors: Weimin Huang, Yonggang Ji, Yiming Wang and Weifeng Sun

Received: 21 November 2023
Revised: 30 December 2023
Accepted: 6 January 2024
Published: 9 January 2024

1. Introduction

High frequency surface wave radar (HFSWR) can provide the capabilities of over-the-horizon detection and ocean remote sensing by transmitting vertically polarized electromagnetic waves working in the high-frequency band of 3–30 MHz. It is an integrated maritime surveillance system because of its notable features of high Doppler frequency resolution, long distance, and all-day adaptability [1]. However, the target detection performance of the HFSWR system depends highly on the distribution of external environmental noise, the principal components of which consist of cosmic noise, man-made noise, and atmospheric noise [2]. Especially in the high frequency (HF) band, this external environment noise has a complex behavior that varies with geographic location, time of day, season, solar activity cycle, and operating frequency [3,4]. Previous studies generally considered that HF external environmental noise is omnidirectional in azimuth [5,6]. However, the spatial distribution of the external environment's noise intensity is directional due to severe weather on the sea surface (such as lightning and typhoons) or human factors (such as industrial or residential areas), called directional noise [7–10]. As for radar systems, detecting weak targets of interest emerging into directional noise is a new challenge.

HF external environment noise has been an important research subject. In the 1930s, many measurements and research on HF noise were started in Europe [11–14]. However, the results are controversial due to the limitations of the equipment and the lack of standardization of measurement methods. HF noise was generally modeled as Gaussian noise, color noise, or a mixture of pulse noise and discrete interference components [15]. Most of the modeling and measurement experiments of HF external environmental noise were focused on its temporal or statistical characteristics, with little consideration of its spatial directional distribution. The standard HF environment noise model was released by the International Telecommunication Union (ITU) in 1990, providing only a fairly rough result for noise distribution [16,17]. Based on the ITU model, Kotaki first developed an HF external environmental noise model based on the global lightning strike activity distribution [18]. Unfortunately, both the Kataki and ITU models failed to provide information about noise directionality distribution. However, a strong directional characteristic is supported by observations from the HFSWR receiver [10]. Coleman first proposed an HF directional noise model based on global maps of lightning strike occurrence and ray tracing propagation methods [7]. Pederick combined background ionosphere and ionospheric absorption models based on the Coleman model, which can simulate the directional noise more accurately [8]. The simulated results agree well with the Jindalee Operational Radar Network (JORN) radar measurements, matching the results more closely than the standard ITU noise model. Gibson and Arnett carried out some research on the directional distribution of HF noise at a measuring site in Southern England [19]. The results showed the greatest asymmetry in noise intensity during the spring or summer evening, and the results were also generally consistent with the expected distribution of atmospheric noise caused by thunderstorm activity at that time.

At HF, external environmental noise originates mainly from three sources, as shown in Figure 1. The atmospheric component is driven by lightning strikes, which can be separated into two components: a local component (which propagates via ground waves or line-of-sight, for example, when local thunderstorm activity is within 100 km of the HFSWR receiver) and an ionospheric component. The ionospheric component results from the superposition of many lightning strikes across the globe. The electromagnetic radiation from lightning strikes will be reflected in the ionosphere [20,21]. Under certain propagation conditions, this portion of radiation can be received by the radar receiver after a second reflection via the ionosphere. Man-made noise is caused by electrical and electronic equipment, power transmission lines, combustion engine ignition, power line telecommunications, and switching power. Due to the high equipment density in cities and their proximity, noise levels are high [22]. This noise reaches the receiver by direct coupling, line-of-sight, or groundwave propagation, depending on distance and frequency. In addition, the effect of man-made noise propagated via ground waves depends on the location of the noise source relative to the radar; it has location uniqueness [23]. Another source is cosmic noise, which originates from extraterrestrial space and needs to propagate through the ionosphere. This noise is only present at higher frequencies or high elevation angles, and electromagnetic waves at lower frequencies and low elevation angles are attenuated by the ionosphere and cannot penetrate the ionosphere.

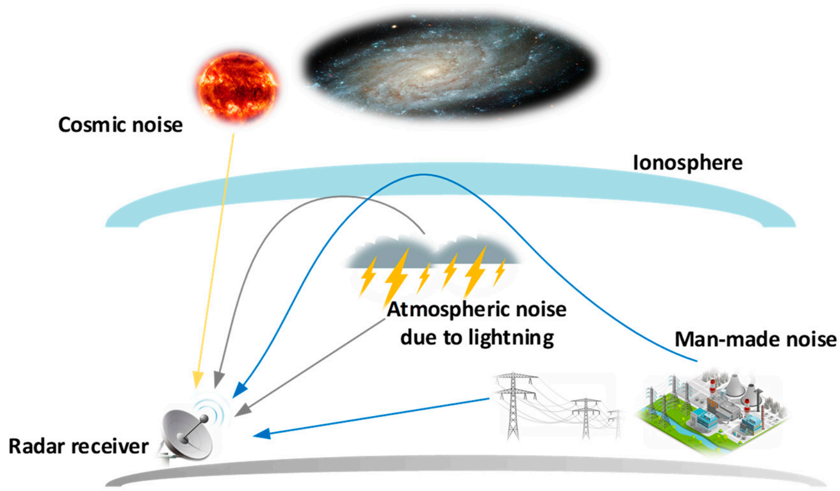

Figure 1. Source of directional noise.

Different from clutter and interference that affect the performance of the HFSWR system, directional noise covers all the Doppler shift units. In other words, directional noise can be considered a kind of main lobe broadband noise interference. Currently, the research on HFSWR narrowband interference suppression by signal processing methods is relatively in-depth, mainly including frequency domain notch methods [24], parameter estimation methods [25], characteristic subspace spatial-based filtering methods [26], adaptive beam forming methods [27], blocking matrix preprocessing methods [28], eigenprojection matrix preprocessing methods [29], and blind source separation technique [30]. Adaptive beamforming technology can automatically form a notch in the interference direction. However, this technique does not remove the target information from the interference covariance matrix when designing the weighted vector of the optimal filter, and it needs to know the target direction information; otherwise, the target will self-eliminate. The essence of the blocking matrix preprocessing method is to preprocess the received data through the blocking matrix to suppress the main lobe interference signal, but the blocking matrix construction process requires a high degree of accuracy in the measurement of the arrival angle of the main lobe interference. In addition, since the main lobe interference is located in the same main lobe beam as the target, the blocking matrix preprocessing suppresses the main lobe interference while the target self-cancellation may occur. The essence of the feature subspace projection preprocessing method is based on the processing of the eigenvalues of the covariance matrix of the array data, extracting the non-target interference samples to estimate the interference covariance matrix, and designing the optimal spatial filter to achieve interference suppression. However, since the main lobe interference is located in the same main lobe beam as the target, it still leads to the phenomenon of target self-cancellation. The blind source separation technique is based on the statistical properties of the source signals, and only the observed signals are used to separate the different echo source signals to design the optimal spatial filters for interference suppression. However, the separation effect of the blind source separation algorithm is related to the direction difference between the target and the interference, which has a good suppression effect on the interference in the non-target direction. Therefore, for the main lobe noise interference, it is difficult to completely separate the interference from the target, which will still lead to the self-elimination of the target.

Due to the unique properties of directional noise, existing methods cannot be applied directly and need to be improved accordingly. In [31], the wideband linear array white noise is reduced by a judiciously designed spatial transformation followed by a bank of high-pass filters. J. Xiong et al. [32] presented a cascade model consisting of a noise estimation network based on U-Net and a recognition network based on MSCANet. It can recognize the working mode of the radar in a harsh noise environment. There are also several works to improve anti-interference from the perspective of transceiver devices, antenna design, and polarization domain, e.g., [33–35]. Y. Xu et al. [36] proposed a method to achieve anti-jamming using a priori information about the external environment. However, it is difficult to obtain accurate, a priori information about the external environmental noise faced by HFSWR. Yao investigated a transient interference suppression method based on a space-time cascade and an optimal sample selection strategy based on information geometry through interference correlation in the spatial domain [37]. G. Li et al. [25] developed a wideband noise suppression method based on de-chirping and double subspace extraction. Chen proposed a suppression method based on fractional Fourier change and second-order blind identification [38].

The most typical difference between directional noise and receiver internal thermal noise is that it has spatial information. Therefore, we focus on the suppression of direction noise for HFSWR systems from the perspective of spatial cancellation. Directional noise has complex sources and propagation paths, and its amplitude is 10–15 dB higher than conventional noise floor, which will submerge weak targets, such as high-speed moving aircraft, unmanned aerial vehicles, or targets with very small RCS. For signal processing, directional noise elevates the noise base. Under the same detection threshold, weak targets cannot be detected, which will have a serious impact on the detection and tracking of targets [39,40]. It is worth noting that directional noise will reduce the target perception capability and robustness of the HFSWR system, which has not been considered or analyzed in previous studies.

We investigate the characteristic analysis of the directional noise of HFSWR using measured data for the first time. Spatial and eigenvalue distribution characteristics are analyzed, guiding the design of a directional noise suppression algorithm. The spatial property affects how to reject the target component, and the eigenvalue distribution attribute affects the covariance estimation. Currently, main lobe cancellation (MLC) is the widely used spatial suppression method [28,41]. Zhang proposed a spread clutter estimated canceller (SCEC) algorithm based on clutter spatial distribution characteristics, which achieves clutter cancellation by estimating clutter in the main lobe with clutter in the side lobe [24]. The core of the MLC is to estimate the information about the other directions of the non-expected component to cancel the non-expected component of the looking direction under the reasonable design of the blocking matrix. The limitation of the MLC is that the canceled, non-expected component needs to be strongly correlated in the spatial domain, which can result in good performance. However, directional noise has both random properties similar to thermal noise and directional properties similar to clutter, with low correlation in the spatial domain. The performance of traditional spatial methods for clutter suppression will be degraded when faced with directional noise. It can estimate the directional noise more accurately under the condition of low correlation in the spatial data and effectively suppress the directional noise while improving the signal-to-noise ratio (SNR) of the target.

The main contributions are described as follows:

1. The directionality of the external environmental noise received by the HFSWR was demonstrated using measured data. The results confirmed that the directional noise level is generally increased by 10 to 15 dB compared to the traditional noise floor level, and weak targets masked by the directional noise would be difficult to detect, which seriously affected the performance of HFSWR;
2. The spatial characteristics of directional noise were analyzed based on measured data. Then, a correlation analysis method based on angle-Doppler joint multi-eigenvector synthesis was proposed to analyze the spatial correlation of directional noise. The results demonstrated that directional noise has much higher correlation coefficients than omnidirectional noise. On this basis, an algorithm based on sliding main lobe cancellation (SL-MLC) for directional noise based on SSNSF was proposed, which could estimate directional noise more accurately under the condition of low spatial domain correlation;
3. In addition, compared to the standard MLC method, DBF, and JDL, the proposed algorithm could suppress directional noise more effectively, which met the requirements of the target detection threshold.

This paper is organized as follows. Firstly, the data model of the HFSWR system and the causes of directional noise generation have been introduced in Section 2. In Section 2.3, a correlation analysis method based on angle-Doppler joint multi-eigenvector synthesis is proposed to analyze the spatial correlation of directional noise. On this basis, the framework of SL-MLC is proposed, and the analyses of the impact of amplitude-phase errors are shown in Section 3. Section 4 describes the experimental results of the SL-MLC algorithm and presents an analysis of the results. Finally, Section 5 gives the conclusion of this study.

2. Data Model and Directional Noise Statistic Analysis

Directional noise differs from Gaussian white noise in that it has spatial information. Utilizing a spatial domain adaptive algorithm to suppress HFSWR directional noise requires an accurate analysis of its spatial characteristics. The tools employed to research directional noise all use data in the form of spatial covariance matrices. We analyzed the underlying environmental noise characteristics based on the information contained in the eigenvalues and eigenvectors of the spatial covariance matrix.

2.1. Signal Model

The HFSWR array configuration is shown in Figure 2. Consider an N-element uniform linear array, and the carrier wavelength λ, the element spacing is d. The m-th sample of echo data $\boldsymbol{x}(m)$ can be expressed as:

$$\boldsymbol{x}(m) = \boldsymbol{s}(m) + \boldsymbol{c}(m) + \boldsymbol{n_o}(m) + \boldsymbol{n_d}(m), \quad (1)$$

where $\boldsymbol{s}(m)$ indicates the signal of interest, $\boldsymbol{c}(m)$ indicates the clutter, $\boldsymbol{n_o}(m)$ indicates the omnidirectional noise, and $\boldsymbol{n_d}(m)$ indicates the directional noise.

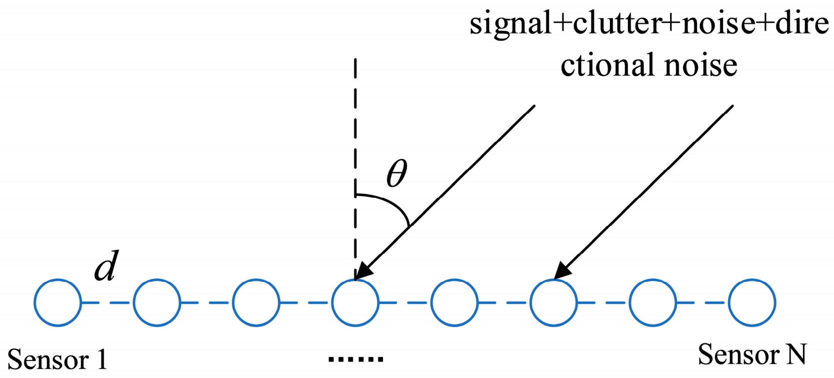

Figure 2. Uniform linear array.

Figure 3a shows the range-Doppler spectrum of HFSWR, which contains ionospheric clutter, sea clutter, ground clutter, noise, and other components. After DBF processing and the range-Doppler map with the beam pointing at $-18°$ and $27°$, as shown in Figure 3b, we can observe the difference in noise base intensity appearing in two directions. When the beam direction is $27°$, the noise base intensity in the whole HFSWR detection area is significantly higher than when the beam direction is $-18°$. The elevation of the noise floor will have a serious impact on target detection and tracking. Figure 3c,d displays the angle-Doppler map and Doppler profile of the 125th range bin. From Figure 3c, we can see that directional noise covers all Doppler units and occupies some angle units. Figure 3d shows Doppler profiles for a beam pointing of $27°$ and a beam pointing of $-18°$. We can see that over the entire Doppler frequency range, the noise base intensity at $27°$ is approximately 15 dB higher than that at $28°$. Theoretically, all clutter, interference, and target data contain directional noise components, but directional noise is not the main component of these data. It is hard to separate them. If the selected data contains more clutter and interference, this will produce serious errors in the research of directional noise. Therefore, we choose the data without clutter and interference, only directional noise, targets, and omnidirectional noise. The purpose of doing this is to more accurately extract and analyze the features of the directional noise itself without being influenced by other components. Therefore, based on the above considerations, the model can be simplified and expressed as:

$$\boldsymbol{x}(m) = \boldsymbol{s}(m) + \boldsymbol{n_o}(m) + \boldsymbol{n_d}(m). \quad (2)$$

In HFSWR, the omnidirectional noise can be modeled as zero-mean Gaussian distributed noise, and the signal of interest as $\boldsymbol{s}(m) = \sqrt{N}A(m)\boldsymbol{a}_s$, where $\boldsymbol{a_s}$ is a vector that contains the direction of the arrival of the signal of interest $A(m)$, which is the amplitude of the signal of interest. Therefore, the covariance matrix of the echo can be written as:

$$\boldsymbol{R} = E\left[x(m)x^H(m)\right] = N\sigma_s^2\boldsymbol{a}_s\boldsymbol{a}_s^H + \sigma_{n_o}^2\boldsymbol{I} + E\left\{\boldsymbol{n}_d(m)\boldsymbol{n}_d^H(m)\right\}, \quad (3)$$

where $\sigma_s^2 = |A(m)|^2$ is the power of the signal, $\sigma_{n_o}^2$ is the omnidirectional noise power, $\boldsymbol{I}$ denotes the identity matrix, $E\{\boldsymbol{n}_d(m)\boldsymbol{n}_d^H(m)\}$ indicates the directional noise covariance matrix, and $(\cdot)^H$ denotes the Hermitian transpose.

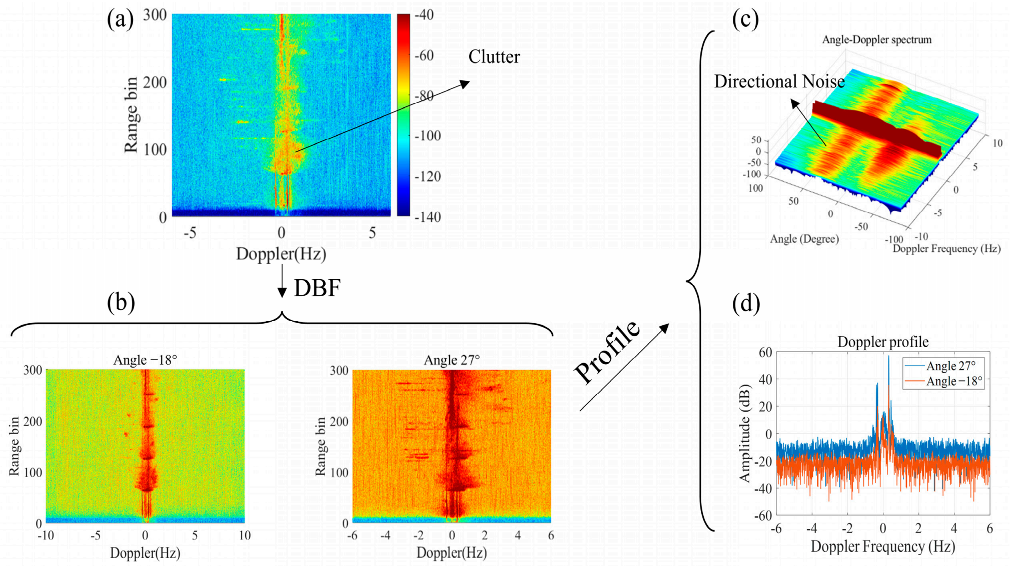

Figure 3. Directional noise multidimensional distribution. (**a**) range-Doppler map. (**b**) range-Doppler map with the beam pointing at −18° and 27°. (**c**) angle-Doppler map of the 125th range bin. (**d**) Doppler profile at angles 27° and −18° of the 125th range bin.

2.2. Data Sets Received by HFSWR

The measured data is obtained by a HFSWR system located in Weihai, China, which consists of 16 element antennas. The main parameter information of the HFSWR system is shown in Table 1. Figure 4 shows the location of radar sites and the direction of beams. Multiple independent beams are formed from the 16 array elements, covering a 100° arc centered on the radar's boresight. The beam pointing is shown as the red solid line in the figure, and the red dashed line is the center of the beam. The center of the radar beam points to the Bohai Ocean region, which has fewer lightning activities and other HF environmental noise sources. However, the radar's positive and negative beam directions are pointed inland, where there are many industrial areas, power plants, and other man-made HF noise sources. This has a strong correlation with the formation of directional noise.

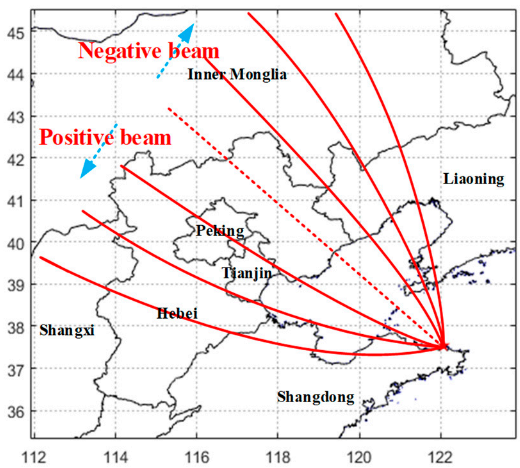

Figure 4. Map depicting the location of radar sites and the direction of the beams.

Table 1. The related parameters of the applied HFSWR system.

Properties	Specification
Elements	16
Frequency bandwidth	60 kHz
Carrier frequency	5.4 MHz
Coherent integration time	144 s
Waveform	FMICW
Range resolution	1.5 km
Doppler frequency resolution	6.94 mHz
Transmit power	8 kw

In theory, the HF noise power should be uniform in all directions. Due to the particular geographic location of the HFSWR antenna array and other factors, directional noise is present in the echo data. Figure 5a shows the azimuth-Doppler map of directional noise. As we can see, the directional noise occupies almost all the Doppler bin and exists only in the observed direction around 18~40°, and its amplitude is much lower than the clutter but 10–15 dB higher than the noise floor. As shown in Figure 5b, we calculate the average power of the noise in different directions. We can see that the average power of the noise is unevenly distributed over the range of HFSWR detection angles and has large fluctuations in different angle ranges. This is consistent with the expected spatial distribution of environmental noise caused by man-made factors.

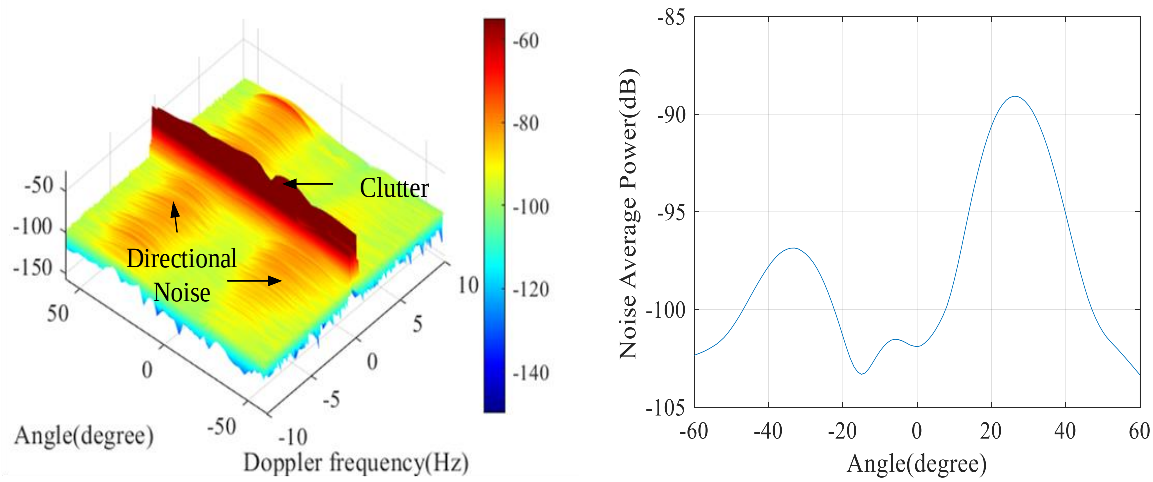

(**a**) (**b**)

Figure 5. Measured HFSWR data contaminated by directional noise: (**a**) azimuth-Doppler map of directional noise; and (**b**) average power of noise in different directions.

2.3. Spatial Characteristics of Directional Noise

The spatial characteristics are the basis for designing the directional noise suppression algorithm. For HFSWR clutter, the main lobe cancellation method is an effective method to suppress clutter for the situation of the target submerged by the main lobe of clutter. This method uses spatial correlation to obtain target-free training data to achieve clutter cancellation [42]. Therefore, if the MLC method is to be applied to the HFSWR directional noise suppression problem, the spatial characteristics need to be analyzed.

As shown in the azimuth-Doppler map of directional noise in Figure 5a, the directional noise occupies a certain direction, which is about 18° to 40°. However, with the same array parameters, the main lobe width of the target is 12°, which differs from the spatial characteristics of the directional noise. The target can be blocked by a well-designed blocking filter.

The core of the MLC method to suppress directional noise is to estimate in the looking direction with the directional noise in the other direction, and the directional noise under test can be canceled by the estimation [43]. Therefore, to accurately estimate the directional noise of the main lobe, the directional noise is required to have a certain spatial correlation. The current correlation analysis methods are all based on the sub space eigenvector method under the clutter background. The sampled covariance matrix is eigen-decomposed. The eigenvectors corresponding to the largest eigenvalues are obtained to form the clutter subspace to represent the clutter characteristics of the current angle bin. The correlation coefficients of the corresponding eigenvectors in the clutter subspace between different angle bins are used to quantitatively analyze the spatial correlation of the clutter. However, the method can express the spatial correlation of clutter well in the case of the absolute predominance of clutter in the localized processing region (LPR). For directional noise, which is not dominant in LPR, the directional noise subspace composed of eigenvectors of a single eigenvalue cannot fully represent the directional noise property. Consequently, this paper proposes a correlation analysis method based on the synthesis of multiple eigenvalues. Based on the difference between the eigen-distribution of directional noise and omnidirectional noise, the characteristics of the underlying noise environment are analyzed from the information contained in the spatial covariance matrix. Thus, we can obtain the optimal sub space eigenvectors that can represent the directional noise characteristics of LPR.

This section first analyzes the eigenvalue spectrum characteristics of directional noise and omnidirectional noise. Assuming an LPR contains only omnidirectional noise or directional noise, which can be expressed as:

$$\boldsymbol{X}_{LPR}(m) = \begin{cases} \boldsymbol{n}_o(m) \\ \boldsymbol{n}_o(m) + \boldsymbol{n}_d(m) \end{cases}. \tag{4}$$

Estimating the statistical covariance matrix using the sample covariance matrix:

$$\hat{\boldsymbol{R}}_{LPR} = \begin{cases} \hat{\boldsymbol{R}}_{no} \\ \hat{\boldsymbol{R}}_{no} + \hat{\boldsymbol{R}}_{nd} \end{cases}, \tag{5}$$

where $\hat{\boldsymbol{R}}_{no}$ denotes the covariance matrix of LPR containing only omnidirectional noise, and $\hat{\boldsymbol{R}}_{no} + \hat{\boldsymbol{R}}_{nd}$ denotes the covariance matrix of LPR containing both omnidirectional and directional noise. Assuming that $\lambda_1 \geq \lambda_2 \geq \cdots \lambda_K$ and $\rho_1 \geq \rho_2 \geq \cdots \geq \rho_K$ represent the eigenvalues of $\hat{\boldsymbol{R}}_{no}$ and $\hat{\boldsymbol{R}}_{no} + \hat{\boldsymbol{R}}_{nd}$, respectively, then the eigenvalue difference $\boldsymbol{s}$ can be expressed as:

$$\boldsymbol{s}(i) = \rho_i - \lambda_i \qquad i = 1, 2, \cdots K, \tag{6}$$

where $\boldsymbol{s}$ denotes the difference in the eigenvalues of the covariance matrix of different LPRs. Under the same radar operating state, the eigenvalue difference can reflect the degree of similarity between different components. When the difference value is smaller, it means a higher degree of similarity. When the difference in the eigenvalues is larger, it means that the difference in the selected LPR components is larger.

The LPR where the directional noise and omnidirectional noise regions are located is selected separately for comparison, and the results of the eigenspectrum distribution in descending order are shown in Figure 6a. We can see that the eigenspectrum has an obvious inflection point, which occurs at the 5th eigenvalue. After that, the eigenvalue distribution gradually becomes stable and almost coincides with the eigenvalue spectrum of the omnidirectional noise. Figure 6b shows the distribution of eigenvalue differences. It can be seen that the decline rate of the first five eigenvalues is significantly higher than that of the subsequent eigenvalues. Therefore, we can conclude that the eigenvectors corresponding to the first 5 eigenvalues can represent the directional noise characteristics of the current LPR. Of course, the eigenvalue analysis method needs to be appropriately adapted to the actual situation of the radar array configuration.

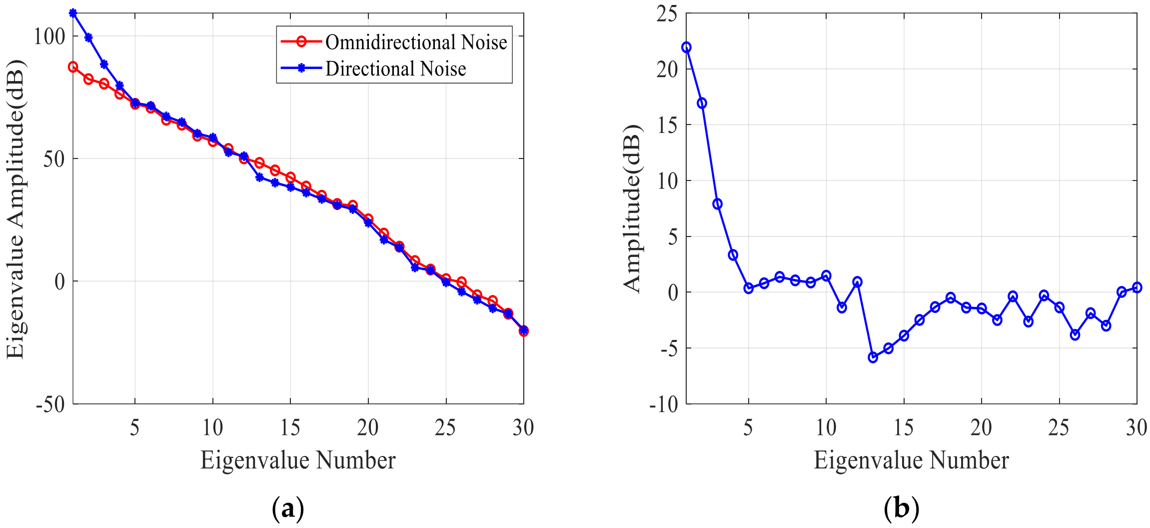

Figure 6. Eigenvalue properties of measured directional noise and omnidirectional noise. (**a**) Directional noise and omnidirectional noise eigenvalue distribution. (**b**) Difference in eigenvalues between directional noise and omnidirectional eigenvalues.

Based on the above analysis, the improved correlation analysis method based on multi-eigenvalue synthesis is operated as follows:

(1) Select K two-dimensional range-Doppler LPR for the one-angle bin and convert into column vectors $\boldsymbol{X}_{LPR}^{k} = [x_1, x_2, \ldots, x_L], k = 1, 2, \cdots, K$, where $L = m \times n$ denotes the size of the LPR, m is the number of the range bin, and n is the number of the Doppler bins;

(2) Calculate the directional noise spatial covariance matrix $\boldsymbol{R}_x$:

$$\boldsymbol{R}_x = 1/K \sum_{k=0}^{K-1} \boldsymbol{X}_{LPR}^{k} {\boldsymbol{X}_{LPR}^{k}}^{H}; \tag{7}$$

(3) Perform the eigenvalue decomposition of $\boldsymbol{R}_x$, and obtain L eigenvalues $\lambda_1, \lambda_2, \cdots, \lambda_L$ and the corresponding normalized eigenvectors $\boldsymbol{\zeta} = [\zeta_1, \zeta_2, \cdots, \zeta_L]^T$;

(4) Calculate the first N_e eigenvalues and eigenvectors weighed by the statistical results to obtain an integrated eigenvector ς to represent the directional noise characteristics of the current angle bin, where w is the weight:

$$\varsigma = \sum_{i=1}^{N} w_i \lambda_i \zeta_i, i = 1, 2, \cdots N_e; \tag{8}$$

(5) Perform the same process on the L_A angle bin and obtain L_A eigenvectors $\boldsymbol{\xi} = \left[\varsigma_1, \varsigma_2, \cdots, \varsigma_{L_A}\right]^T$;

(6) Based on the eigenvectors obtained in (5), calculate the correlation coefficient ρ_{ij} for the angle bin under test and other angle bins:

$$\rho_{ij} = \varsigma_i^H \varsigma_j, \qquad i, j = 1, 2, \cdots, L_A. \tag{9}$$

Then, we analyzed the spatial correlation of directional noise using a set of measured data. All the received data are successively processed by pulse compression, Doppler, and digital beamforming. When performing digital beamforming processing, the spatial window functions of the whole beams are 25 dB Chebyshev windows. The whole spatial zone (from $-54°$ to $54°$) is divided into 37 beam cells ($3°$ interval). The reference direction is $28°$, and the size of the LPR is 9*9. The Doppler samples are selected at the center of

4 Hz, and the range samples are selected at the center of the 40 range unit. To better express the directional noise information utilized by the limited LPR samples, we selected $2mn$ samples in a one-angle bin.

Figure 7 gives the results of the correlation coefficient of the directional noise. We can see that where the directional noise is more aggregated, its correlation is stronger, about 20°, which is wider than the width of the target main lobe. It means that the directional noise in this azimuthal range is homogeneous with the directional noise in the main lobe. It should be noted that the correlation coefficient is small in the azimuthal range of about −50° to 20°. This is because only omnidirectional noise exists in this azimuthal range, resulting in a very low correlation, which is in accordance with the actual physical laws.

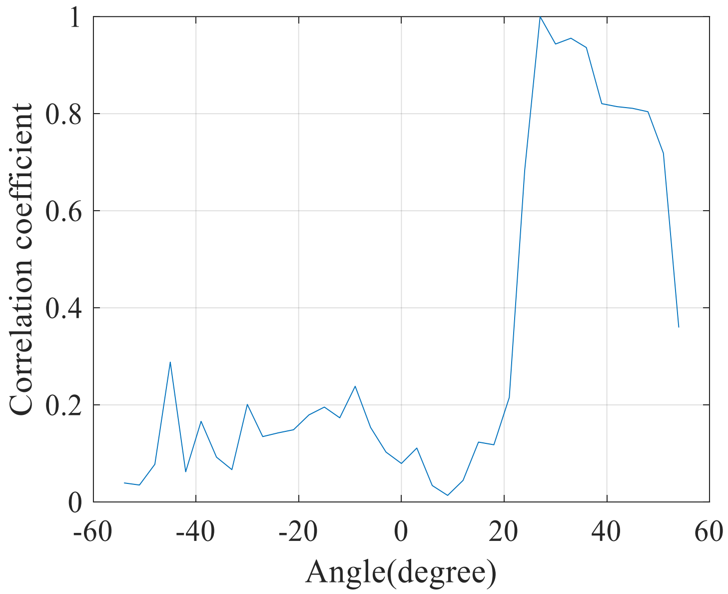

Figure 7. Directional noise correlation coefficient.

According to the above analysis, we can conclude that the MLC method can suppress directional noise in the background of HFSWR. In the next section, we develop an effective directional noise suppression algorithm based on these results.

3. Proposed Framework: SL-MLC

The MLC method is developed from the generalized side lobe canceler (GSC) proposed by Griffiths [44] and is mainly applied to adaptive acoustic noise cancellation at first [45]. With the development of ocean remote sensing technology, it is further applied to ionospheric clutter suppression, sea clutter suppression, and target detection of HFSWR. The principle of the MLC method is to use the blocking matrix to obtain target-free training data to estimate the covariance matrix of the noise or clutter. The ionospheric clutter and sea clutter in HFSWR have a strong correlation in the spatial dimension, so we can use the clutter information in other directions to estimate the main lobe direction to achieve clutter suppression.

There are also similar characteristics for direction noise in HFSWR. In addition, the training data used to estimate directional noise information cannot contain the target information to prevent target self-cancellation. Through previous studies, the blocking matrix is composed of a single-notch space filter (SNSF), which can achieve the separation of target and clutter. In the situation of a clutter hybrid with multiple targets, the system requires a large degree of freedom. To ensure that the system has enough freedom, an auxiliary channel is established by way of a sliding sub-array to obtain auxiliary data. However, directional noise has both the randomness property of noise and the directional distribution property of clutter, so how to estimate the directional noise more effectively and accurately based on its multiple properties is the key problem of directional noise elimination. To solve this problem, we propose an SL-MLC method that combines mathematical and statistical theories to achieve the suppression of directional noise. The main principle of the SL-MLC method is to design the blocking matrix according to the main lobe width and beam interval to achieve more accurate directional noise estimation.

3.1. Slide Single-Notch Space Filter

Through previous research, an SNSF is usually chosen as the blocking matrix using the least P-norm FIR filter to block the target information [24]. However, the conventional SNSF method for estimating directional noise is not precise. As is known, the MLC method's performance depends on the accuracy of the covariance matrix estimation of directional noise. To solve this problem, we proposed a directional noise suppression method based on SSNSF by utilizing multiple properties of directional noise. The structure diagram of SSNSF to achieve directional noise estimation is shown in Figure 8.

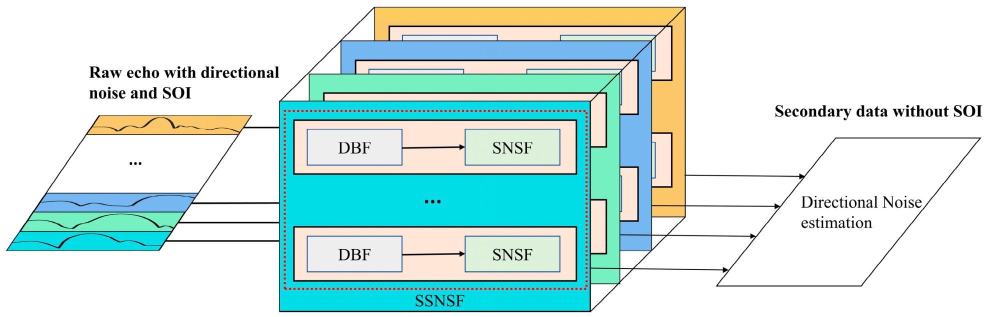

Figure 8. The structure diagram of the proposed SSNSF.

SSNSF is a combination of the directional noise spatial characteristics, the spatial characteristics of the target, the configuration of the antenna array, and the structural characteristics of the SNSF itself. SSNSF is mainly considered in two aspects: first, the sliding parameters are designed according to the antenna array configuration and beam parameters; second, the SNSF filter is designed according to the information of the target parameters. Corresponding to different system operating frequencies, the SNSF can be obtained in different directions by the phase rotation method.

The responses of digital beam forming (DBF) and SSNSF are shown in Figure 9 with the array elements N = 16 and N' = 10, and the main lobe direction is 2°. The entire spatial zone (from $-90°$ to 90°) is divided into 91 beam cells (2° interval), and the main lobe width of the array is 12°. Hence, a single SNSF slides six times within the main lobe to form the SSNSF. However, the beam interval cannot be too small, which will lead to higher computational costs. So, in practice, the empirical beam interval is 3°. The SNSF slides within the width of the main lobe based on the beam spacing (red arrow pointing) in turn, and the red, blue, and green lines represent the SNSF at different sliding moments. The depth of the filter should be deeper than the target power to completely block the target component, and careful design of the SSNSF is required to ensure the filtering effect.

3.2. Signal Model of Directional Noise Excision

In the SL-MLC algorithm, the data is divided into two pathways. One main channel, which performs digital beamforming of the data by fixed static weighting, is the main lobe pointing in the direction of interest. The other is an auxiliary channel, which first filters out the signal components corresponding to the direction of the main lobe by SSNSF to ensure that the residual components do not contain the target component and prevent the target from self-canceling. Then the direction noise information obtained in the sidelobe is used to estimate the direction noise information of the main lobe. Finally, directional noise cancellation is realized by using the difference between the main channel data and the estimated directional noise information of the auxiliary channel. As shown in Figure 10, the upper path has a fixed static weight w_q for digital beamforming to ensure beam direction and sidelobe level. The following path includes the blocking matrix B and the directional noise estimator.

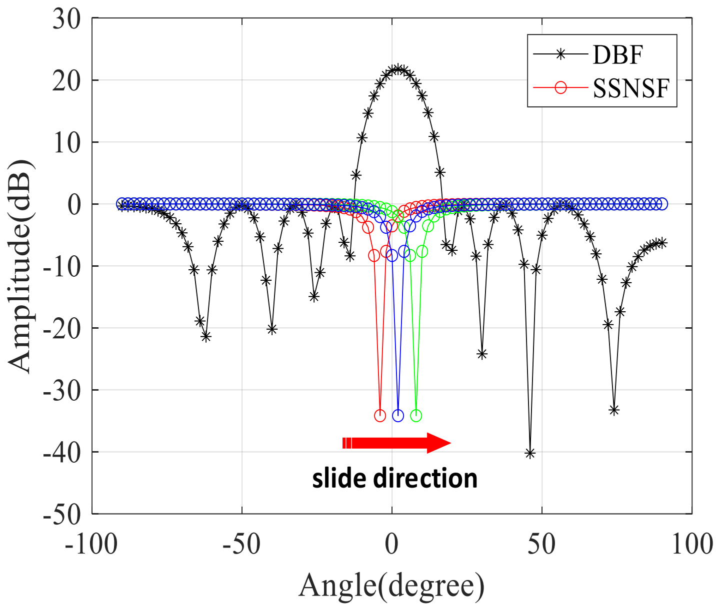

Figure 9. Responses of DBF and SSNSF.

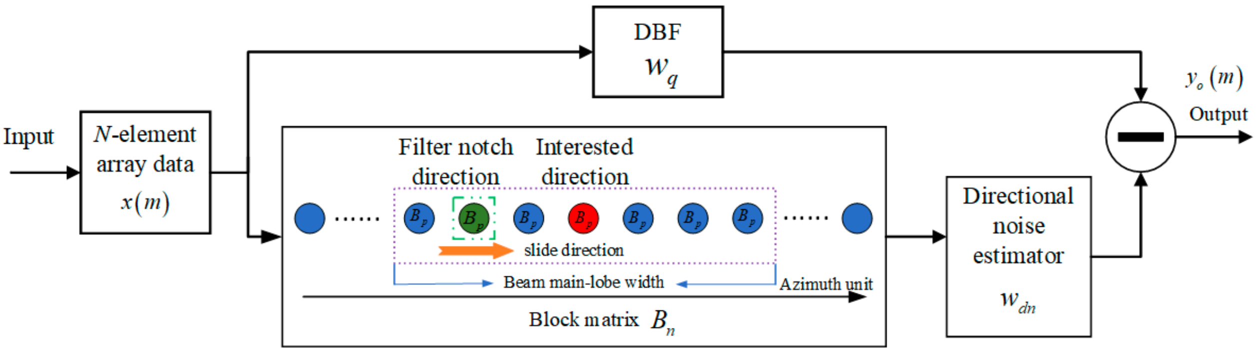

Figure 10. The flowchart of the directional noise suppression procedure is based on the SL-MLC algorithm.

As shown in the framework of the SL-MLC method in Figure 10, the output can be indicated as:

$$\boldsymbol{y}_o(m) = \boldsymbol{w}_q^H \boldsymbol{x}(m) - \frac{1}{P}\sum_{p=1}^{P}\left[\left(\boldsymbol{B}_p \boldsymbol{w}_{dn}\right)^H \boldsymbol{x}(m)\right], \tag{10}$$

where $\boldsymbol{w}_q$ denotes the static weights of the echo obtained by the receiving array, which are the coefficients of DBF in the desired direction. The blocking matrix $\boldsymbol{B_n}$ is used to block the target components to obtain training data, which is composed of SSNSF and p corresponds to different sliding moments. $\boldsymbol{w}_{dn}$ is the adaptive weight vector calculated from the estimated directional noise covariance. Let $\boldsymbol{J} = E\left[|\boldsymbol{y}_o(m)|^2\right]$ denote the cost function, and the optimal weight $\boldsymbol{w}_{dn}$ can be obtained by solving the following unconstrained optimization problems:

$$\min_{w_{dn}} \boldsymbol{J} = \min_{w_{dn}}\left(\boldsymbol{w}_q - \boldsymbol{B}_n \boldsymbol{w}_{dn}\right)^H \boldsymbol{R}_x\left(\boldsymbol{w}_q - \boldsymbol{B}_n \boldsymbol{w}_{dn}\right), \tag{11}$$

where $\boldsymbol{R}_x = \boldsymbol{x}(m)\boldsymbol{x}(m)^H$ is the self-correlation matrix, $\boldsymbol{B}_n = \frac{1}{P}\sum_{p=1}^{P}\boldsymbol{B}_p$. To keep the SNR loss minimized, $\boldsymbol{R}_x$ must only contain directional noise, excluding the target.

Hence, the optimal $\boldsymbol{w}_{dn}$ can be calculated as:

$$\boldsymbol{w}_{dn,opt} = \left(\boldsymbol{B}_n^H \boldsymbol{R}_x \boldsymbol{B}_n\right)^{-1} \boldsymbol{B}_n^H \boldsymbol{R}_x \boldsymbol{w}_q. \tag{12}$$

The expression of signal to interference plus noise ratio (SINR) is as follows:

$$SINR = 10\log_{10}\left(\frac{P_s}{P_n}\right), \tag{13}$$

where P_s represents the power of the target and P_n denotes the average power of directional noise plus omnidirectional noise. In this paper, we take SINR as the evaluation index of algorithm performance.

3.3. Algorithm and Procedure Details

During data processing, firstly, digital beam formation (primary beam) and SSNSF auxiliary beam formation are performed on the channel domain data. The primary beam that extracts the distance to be processed and the auxiliary beam data output from the SSNSF constitute the primary and auxiliary channels, respectively. The main beam can use the Chebyshev weighted pattern to point in a specific direction of the beam to ensure sidelobe characteristics. SSNSF is a notch corresponding to the main beam pointing to a spatial blocking matrix. Define the output of the main channel as $\boldsymbol{y}_{DBF}$, the output of SSNSF as $\boldsymbol{y}_{dif}$, and the result of directional noise cancellation as $\boldsymbol{y}_o$.

For adaptive estimation, the estimated accuracy of directional noise is better as the number of secondary data points is greater. In this case, we divide the receiving array into N_L sub-arrays by sliding $N - N_L + 1$ elements into each sub-array to obtain $N - N_L + 1$ SNSF outputs. First, we define an SNSF with the coefficients $h_j(\theta_p), j = 1, 2, \cdots, N_L$, $p = 1, 2, \cdots, P$ as the block matrix $\boldsymbol{B_n}$ with the θ_p-th sliding moments. Therefore, the block matrix $\boldsymbol{B_n}$ can be expressed as:

$$\boldsymbol{B}_n = [\boldsymbol{B}_1, \boldsymbol{B}_2, \cdots, \boldsymbol{B}_P]^T, p = 1, 2, \cdots, P, \tag{14}$$

$$\boldsymbol{B}_p = [h_1(\theta_p), h_2(\theta_p), \cdots, h_{N_L}(\theta_p)]^T, p = 1, 2, \cdots, P. \tag{15}$$

The output of the i-th block matrix $y_i^n(\theta_p)$ with the θ_p-th sliding moments is shown below:

$$y_i^n(\theta_p) = \sum_{j=0}^{N_L} h_j(\theta_p) x_{i+j}(m), i = 1, 2, \cdots, N - N_L + 1. \tag{16}$$

Then, all the block matrix outputs from the data matrix $y^n(\theta_p)$ with the θ_p-th sliding moments can be expressed as:

$$\boldsymbol{y}^n(\theta_p) = \left[y_1^n(\theta_p), y_2^n(\theta_p), \cdots, y_{N-N_L+1}^n(\theta_p)\right]^T. \tag{17}$$

The total secondary $\boldsymbol{y}_{dif}$ data can be written as follows:

$$\boldsymbol{y}_{dif}(\theta) = \left[\boldsymbol{y}^n(\theta_1), \boldsymbol{y}^n(\theta_1), \cdots, \boldsymbol{y}^n(\theta_p)\right]^T, \tag{18}$$

$$\boldsymbol{y}_{dif} = \frac{1}{P}\sum_{p=1}^{P} \boldsymbol{y}_{dif}(\theta). \tag{19}$$

The output of the i-th DBF can be expressed as:

$$y_i^{DBF} = \sum_{j=0}^{N_L} w_{q,j} x_{i+j}(m) \; i = 1, 2, \cdots, N - N_L + 1, \tag{20}$$

$$\boldsymbol{w}_q = \left(1, e^{-j\frac{2\pi}{\lambda}d\sin\theta}, e^{-j\frac{2\pi}{\lambda}2d\sin\theta}, \cdots, e^{-j\frac{2\pi}{\lambda}(N-1)d\sin\theta}\right)^T. \tag{21}$$

All the DBF outputs form the data vector $\boldsymbol{y}_{DBF}$ as expressed in Equation (22):

$$\boldsymbol{y}_{DBF} = \left[y_1^{DBF}, y_2^{DBF}, \cdots, y_{N-N_L+1}^{DBF}\right]^T. \tag{22}$$

Adaptive optimal weight can be obtained by the minimum mean square error (MMSE), ideally.

$$\boldsymbol{w}_{dn,opt} = \boldsymbol{R}_{dd}^{-1} \boldsymbol{R}_{sd}, \tag{23}$$

$$\boldsymbol{R}_{dd} = \boldsymbol{y}_{dif} \boldsymbol{y}_{dif}^H, \tag{24}$$

$$\boldsymbol{R}_{sd} = \boldsymbol{y}_{dif} \boldsymbol{y}_{DBF}. \tag{25}$$

Thus, the final output after directional noise cancellation can be expressed as:

$$\boldsymbol{y}_o(m) = \left(\boldsymbol{w}_q - \boldsymbol{w}_{dn,opt}\right)^H \boldsymbol{x}(m). \tag{26}$$

Based on the above analysis and derivation, we present the detailed steps of SL-MLC in Algorithm 1 and the flowchart of the directional noise suppression procedure in Figure 10.

Algorithm 1 SL-MLC

Inputs: raw echo $\boldsymbol{x}$ with directional noise;
Outputs: echo data with directional noise removed;
Initialization:
Set the number of sub-arrays N_L, the block matrix coefficients $h(\theta_p)$, $\boldsymbol{B}_p$, $\boldsymbol{B}_n$, and the corresponding sliding moments $\theta_1, \theta_2, \cdots, \theta_P$;

(1) Calculate the i-th block matrix output $y_i^n(\theta_p)$ with the θ_p-th sliding moments using Equation (16);
(2) Calculate all the block matrix output $\boldsymbol{y}^n(\theta_p)$ of all the $N - N_L + 1$ sub-arrays with the θ_p-th sliding moments using Equation (17);
(3) Calculate the total secondary $\boldsymbol{y}_{dif}$ data of all the sliding moments using Equations (18) and (19);
(4) Calculate the DBF outputs $\boldsymbol{y}_{DBF}$ using Equations (20) and (22);
(5) Calculate the self-correlation matrix $\boldsymbol{R}_{dd}$ and the cross-correlation matrix $\boldsymbol{R}_{sd}$ using Equations (24) and (25);
(6) Calculate the final optimal weights $\boldsymbol{w}_{dn,opt}$ for directional noise estimation using Equation (23);
(7) Calculate the final output of SL-MLC $\boldsymbol{y}_o(m)$ using Equation (26);
(8) Repeat steps (1) to (7) for processing the whole range units and beam units.

3.4. Analysis of Amplitude-Phase Error

There are some limitations to the SL-MLC method. In this section, we give an analysis of the amplitude-phase errors' impact on the performance of the algorithm. The SL-MLC method utilizes the auxiliary data based on SSNSF to estimate the directional noise information, so the receiving antenna amplitude-phase error will seriously affect the performance of the algorithm. The amplitude error will change the level of the side lobe response, and the phase error will affect the depth and direction of the SNSF notch. In some extreme situations, the notch of SNSF may even disappear due to the heavy amplitude-phase errors, which will lead to the self-cancellation of the target and make the algorithm fail. Therefore, the compensation of amplitude and phase errors is essential in practical signal processing.

It is generally believed that the amplitude and phase error are quantities independent of the Direction of Arrival (DOA), which is expressed as a fixed error value in mathematical modeling. The modeling of amplitude-phase error is usually described by introducing an azimuth-independent amplitude-phase error vector into the steering vector:

$$\widetilde{\boldsymbol{a}}(\theta) = \boldsymbol{\Gamma}\boldsymbol{a}(\theta), \tag{27}$$

where $\boldsymbol{\Gamma} = diag\{g_1 e^{-j\varphi_1}, g_2 e^{-j\varphi_2}, \cdots, g_N e^{-j\varphi_N}\}$ denotes the amplitude and phase error coefficient, g_i and ϕ_i denotes the amplitude and phase errors, respectively. $\boldsymbol{a}(\theta) = [1, e^{j\frac{2\pi}{\lambda}d\sin\theta}, \cdots, e^{j\frac{2\pi}{\lambda}(N-1)d\sin\theta}]^T$ denotes the steering vector, and $\widetilde{\boldsymbol{a}}(\theta)$ indicates the steering vector with amplitude and phase error.

$$\boldsymbol{\Gamma} = \begin{bmatrix} g_1 e^{-j\varphi_1} & 0 & \cdots & 0 \\ 0 & g_2 e^{-j\varphi_2} & \cdots & 0 \\ \vdots & \vdots & \ddots & 0 \\ 0 & 0 & \cdots & g_N e^{-j\varphi_N} \end{bmatrix} \tag{28}$$

Here, we analyze the effects of amplitude error and phase error on the spatial response of SNSF to guide the algorithm to have better cancellation performance in the actual processing. Figure 11a shows the ideal response and the response under different amplitude error scopes of SNSF, respectively. The amplitude errors are set to be uniformly distributed pseudorandom numbers in the [−1 1] dB, [−2 2] dB, and [−5 5] dB scopes. Figure 11b shows the depth of the notch of the spatial response under different amplitude error scopes of SNSF under 1000 Monte Carlo simulations. The maximum amplitude error scopes are set to [0 10] dB with an interval of 0.1 dB. We can see from the results that the amplitude error will not only affect the side lobe response, causing the inequality of the side lobe response but also lead to a decrease in the depth of the notch of the spatial response. This will cause the main lobe information and side lobe information in the auxiliary channel to increase simultaneously, which is not conducive to the estimation of directional noise. At the same time, the reduction in the depth of the notch will cause the target component to be completely blocked, the target energy after suppression to be seriously reduced, and the signal-to-noise ratio to be lost, which is not conducive to the subsequent target detection. Figure 11c shows the ideal response and the spatial response under different phase error scopes of SNSF, respectively. The phase errors are set to be uniformly distributed pseudorandom numbers in [−1 1] degree, [−3 3] degree, and [−6 6] degree scopes, representing different phase distortions. We can see that the phase error will lead to both a shift in the direction of the notch and a reduction in the depth of the notch. This will cause the target signal from the interested direction to be less suppressed by the filter, and the information of the target signal cannot be completely filtered out. Figure 11d shows the depth of the notch of the spatial response under different phase error scopes of SNSF under 1000 Monte Carlo simulations. The maximum phase error scope is set to [0 10] degrees with an interval of 0.1 degrees. From the results, we can see that the phase error fluctuation will affect the depth of the notch, and in severe cases, it may even prevent the SNSF from acting as a spatial domain filter.

In conclusion, the amplitude and phase errors have a great impact on the notch depth, the side lobe response, and the notch direction of SNSF. Therefore, it is necessary to calibrate and compensate the array antenna before signal processing to ensure the consistency of the amplitude-phase.

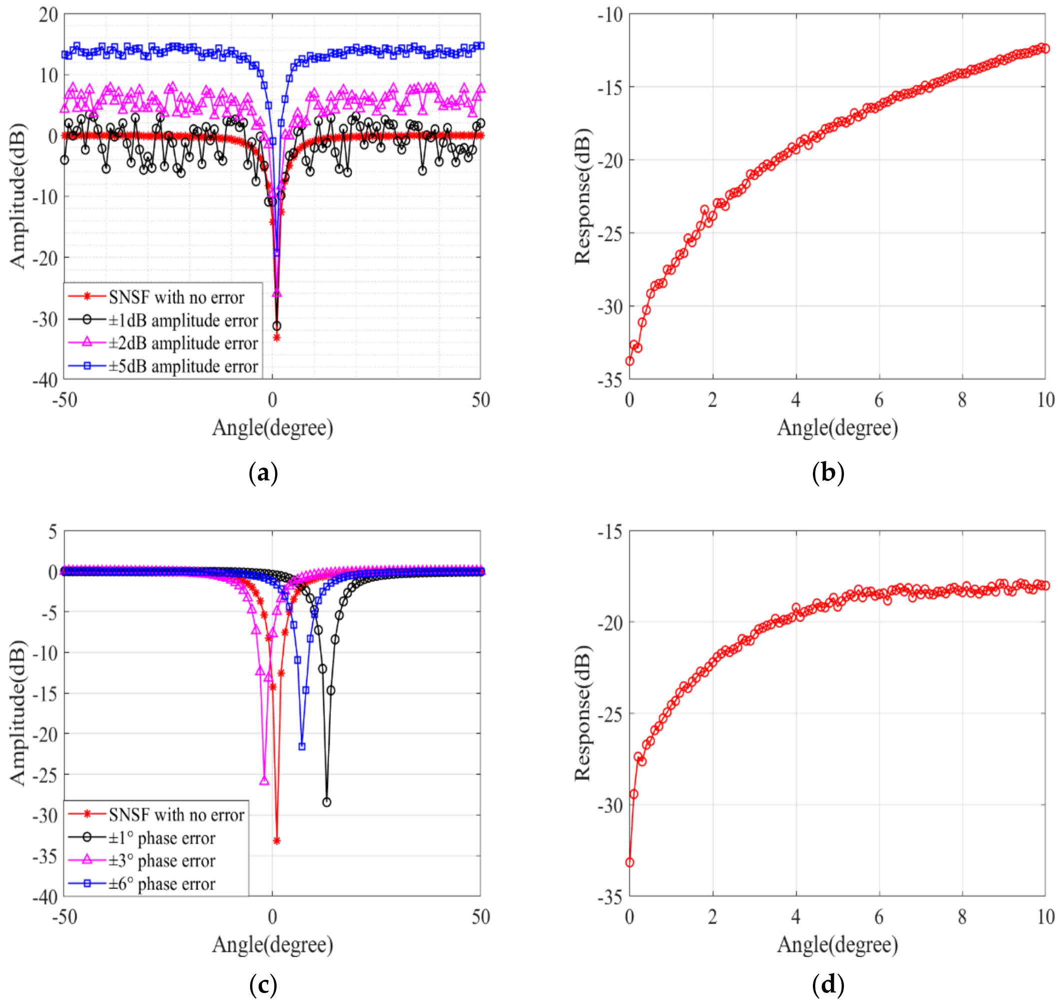

Figure 11. Responses of SNSF with amplitude and phase error. (**a**) Responses of SNSF with different amplitude errors. (**b**) Depth of beam nulling with different phase errors. (**c**) Responses of SNSF with different phase errors. (**d**) Depth of beam nulling with different phase errors.

4. Experimental Results

Directional noise elevates the noise base level. Weak targets will not be detected at the same detection threshold, seriously affecting the performance of the HFSWR system. Hence, in this section, we evaluate the validity and advantages of the proposed method by conducting exhaustive simulations and experimental studies based on measured data. These measured data are the same as the HFSWR data introduced in Section 2.2. Meanwhile, the experimental results were compared with DBF, joint domain localized (JDL), and the conventional MLC algorithm. In the JDL, the size of the local process region is 4×5; four is the number of Doppler cells; and five is the number of angular cells. In a conventional MLC, the number of sub-array elements is 10. For the SL-MLC method, the beam interval is 3° and P is six. The simulated target with the detailed parameters in Table 2 was injected into the directional noise region.

Table 2. Simulation target parameters.

Parameters	Values
Range bin	125
Angle	30°
Doppler frequency	3.5 Hz
SINR	11 dB

It should be noted that the initial purpose of directional noise suppression was to achieve the detection of specific target signals. Currently, the most widely used target detection method is the CFAR algorithm. In the practical HFSWR system, the CFAR method needs to meet a certain detection threshold to ensure a certain false alarm rate. Hence, to better test the performance of the proposed algorithm, the SINR of the simulated target we injected is lower than the detection threshold. In other words, the weak target masked by directional noise cannot be detected.

Figure 12a shows the angle-Doppler map obtained by the DBF method. As shown in the figure, the directional noise is widely distributed in the angle and Doppler domains, completely covering the simulated target information. The angle-Doppler map obtained by the SL-MLC method is demonstrated in Figure 12b. Compared with the DBF method, it is obvious that the directional noise has been suppressed and targets submerged in the directional noise appear.

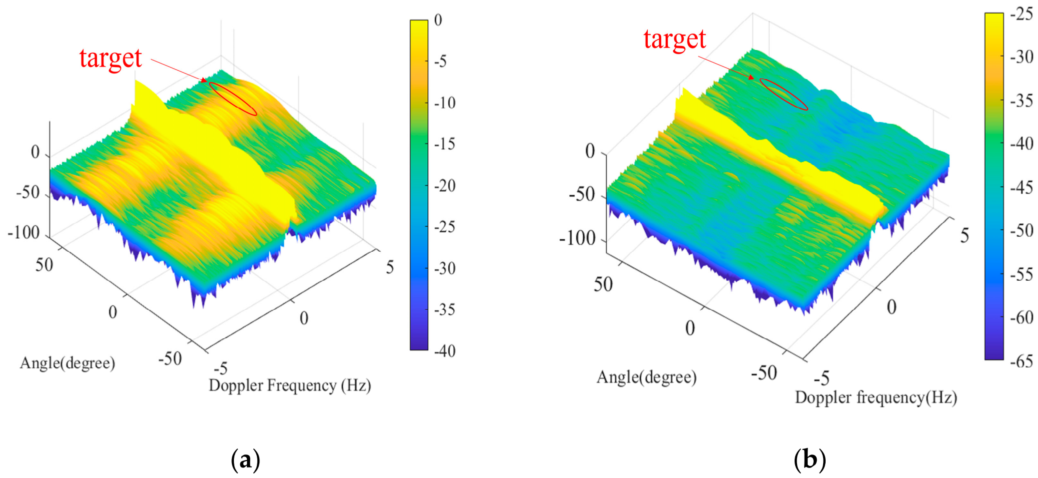

Figure 12. Experimental results using measured data with the simulated target. (**a**) Angle-Doppler map of the DBF method. (**b**) Angle-Doppler map of the SL-MLC method.

Figure 13 illustrates the results of the Doppler profile, which displays the directional noise suppression performance of the proposed algorithm. It can be seen from the results that the performance of SL-MLC is significantly better than the traditional MLC method. Compared with the JDL method, it also has certain performance improvements. However, since directional noise has no space-time characteristics, although the JDL method can suppress directional noise, it also appears to be a false target.

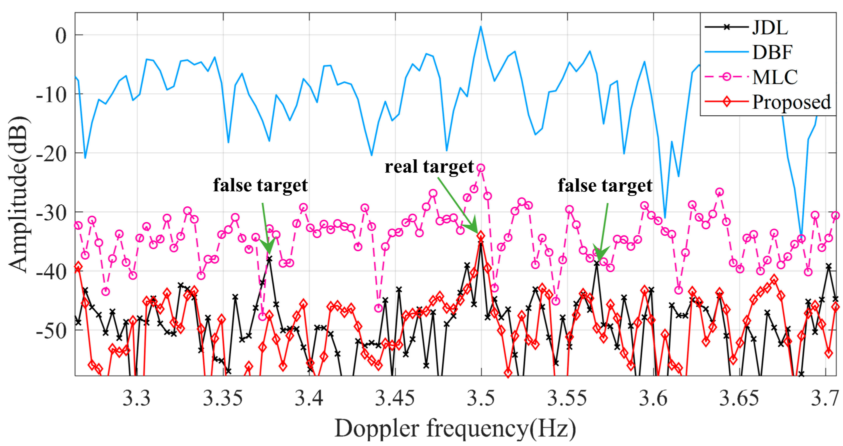

Figure 13. Doppler profile results of the JDL method, the DBF method, the MLC method, and the proposed method.

The SINR improvement, which indicates the improvement of the SINR after directional noise suppression, is introduced to quantitatively evaluate the performance of different algorithms. The expression of SINR improvement is as follows:

$$SINR_{\text{Improve}} = SINR_{\text{after}} - SINR_{\text{before}}, \tag{29}$$

where SINR is calculated using Equation (13).

For HFSWR, it has a high Doppler frequency resolution, but the range resolution is relatively poor. Therefore, the Doppler profile is often used to show the performance of directional noise suppression. In this paper, the SINR improvement was calculated based on the Doppler profile. The average power of directional noise plus omnidirectional noise was calculated by several Doppler bins around the target, and the target power was calculated by the target's Doppler bin.

The SINR improvement results are illustrated in Table 3. For the simulated target, the proposed algorithm had the highest SINR improvement. The SINR improvements of DBF, JDL, MLC, and the proposed method are 0.55 dB, 3.45 dB, 1.67 dB, and 5.42 dB, respectively. After directional noise suppression, the SINR of DBF, MLC, JDL, and the proposed method are 11.55 dB, 12.67 dB, 14.45 dB, and 16.42 dB, respectively. In applications, it is generally considered that the SINR higher than the detection threshold is the target. In a practice radar system, the detection threshold is set to 14 dB according to the empirical value. In this case, only the JDL method and the proposed method are higher than the detection threshold. Thus, target detection can be easily realized. Fortunately, the SL-MLC proposed in this paper can suppress directional noise and improve SINR while protecting target information, which is a great advantage for detecting weak targets submerged by directional noise, such as aircraft targets moving at high speed. Although the method proposed in this paper has little improvement on SINR, it is of great help to improve the sensitivity of HFSWR. It plays an important role in improving the geographical environment adaptability, electromagnetic environment adaptability, and robustness of HFSWR.

Table 3. Signal-to-interference plus noise ratio (SINR) improvement.

Algorithm	SINR (dB)	SINR Improvement (dB)
	Simulated Target	
DBF	11.55	0.55
JDL	14.45	3.45
MLC	12.67	1.67
Proposed algorithm	16.42	5.42

Directional noise has both the random property of noise and the directional distribution property of clutter. The advantage of the SL-MLC method is that it can combine the multiple properties of directional noise to estimate it more accurately. To verify it, we conducted two sets of comparison experiments. Theoretically, the covariance matrix calculated by the blocking matrix without injecting the simulation target represents pure directional noise information. The covariance matrix calculated by the blocking matrix when injecting the simulation target represents the main lobe directional noise that needs to be canceled. Under the same experimental parameters, we use the estimated pure directional noise without injecting the simulated target to replace the estimated main lobe directional noise by injecting the simulated target. Then, the improvement of the target is used as the criterion to judge the accuracy of directional noise estimation. The experimental results are shown in Figure 14. Compared with the MLC method, the target amplitude improved by 4.43 dB before and after the experiment. Hence, the performance of the SL-MLC algorithm is better than that of conventional MLC for directional noise estimation.

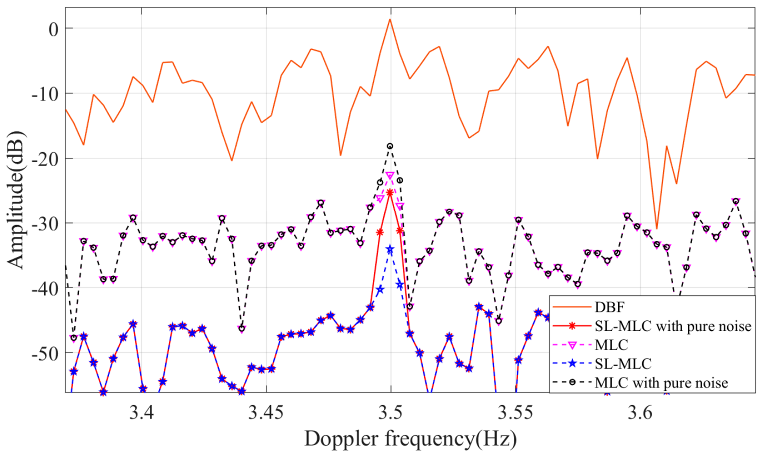

Figure 14. Doppler profile result of directional noise estimation verification of the MLC method and the SL-MLC method.

The SINR after signal processing of injected targets at different SINR values from 5 to 35 dB is shown in Figure 15, which is used to evaluate the performance of the SL-MLC algorithm under different SINRs. The SINR after directional noise suppression by different methods is given by Monte Carlo simulations of 100 trials. The SINR was calculated based on the Doppler profile. In general, the SINR is increasing, with the SINR and magnitude of simulated targets increasing. Initially, when the SINR of the simulated target is very low (<9 dB), all the methods cannot achieve a better performance improvement, and the target cannot be detected. When the simulated targets' magnitude and SINR are relatively large (9–35 dB), SL-MLC expects to uncover the covered targets earlier. Fortunately, the proposed algorithm is better than the comparison algorithm in terms of the overall trend. It is worth noting that when the SINR of the simulation target reaches 25 to 35 dB, the SINR obtained by the conventional MLC method and the DBF method is almost the same. This phenomenon can be attributed to the fact that the rising target amplitude and SINR cause the target energy to be leaked into the side-lobe, leading to target self-elimination. At the same time, the SINR obtained by the JDL method gradually approaches that obtained by the SL-MLC method.

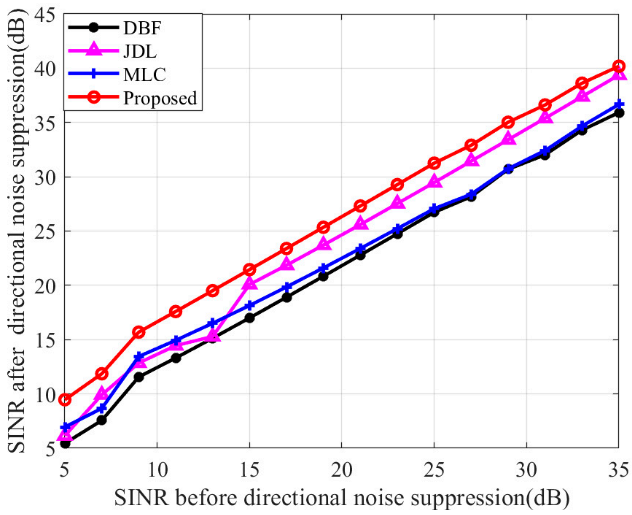

Figure 15. Directional noise suppression results of injected targets with different SINRs.

In conclusion, compared with the DBF method, JDL method, and traditional MLC method, the SL-MLC method achieves a higher SINR improvement after applying directional noise suppression. Therefore, the proposed algorithm can assist in detecting targets with low SINR.

5. Conclusions

In this paper, we propose an improved MLC method based on SSNSF to suppress the directional noise of HFSWR by analyzing the multiple properties of directional noise, combining the spatial domain method and mathematical statistical theory. The spatial distribution characteristics of the external environmental noise of the HFSWR are first discussed. The analysis results of the measured data show that the influence of external factors makes the external environmental noise of HFSWR produce a certain correlation and directional distribution in the spatial domain. The Doppler noise level will be increased by 10–15 dB. Based on the spatial characteristics of directional noise, a correlation analysis method based on angle-Doppler joint multi-eigenvector synthesis is proposed to analyze the spatial correlation of directional noise. The result shows that there are significant differences between directional noise and omnidirectional noise in the eigenvalue domain and that directional noise has much higher correlation coefficients than omnidirectional noise. Therefore, in this paper, we first attempt to use the MLC method to suppress directional noise. To solve the problem of inaccurate estimation of directional noise by the traditional MLC method, an improved MLC directional noise suppression method is proposed. An SSNSF is selected as the blocking matrix, and the influence of amplitude and phase error on the blocking matrix is analyzed. The experimental results show the effectiveness of the algorithm, which can suppress the directional noise and improve the SINR of the target. Compared with the traditional MLC method, our proposed method can estimate directional noise more accurately. In future work, spatial notch filters will be designed based on multiple feature information about the target and directional noise, and directional noise suppression methods will be combined with prior knowledge. On the other hand, we plan to expand our research by designing measurement experiments of directional noise to explore the formation mechanism of directional noise in HFSWR.

Author Contributions: Methodology, validation, writing—original draft preparation, D.X.; software curation, validation, J.L.; supervision, X.Z.; funding acquisition, Q.Y. All authors have read and agreed to the published version of the manuscript.

Funding: This work was supported in part by the National Natural Science Foundation of China under Grant 62031014.

Data Availability Statement: Restrictions apply to the availability of the data, which were used under license for this study. Data are available from the authors withs permission from the Key Laboratory of Marine Environmental Monitoring and Information Processing.

Acknowledgments: The authors thank the Key Laboratory of Marine Environmental Monitoring and Information Processing, Harbin Institute of Technology, China, for data support.

Conflicts of Interest: No author has financial or other contractual agreements that might cause conflicts of interest.

References

1. Ji, Y.; Cheng, X.; Wang, Y.; Sun, W.; Zhang, X.; Jiang, M.; Ren, J.; Li, F. Motion Compensation Method Using Direct Wave Signal for CTSR Bistatic HFSWR. *IEEE Geosci. Remote Sens. Lett.* **2023**, *20*, 3502005. [CrossRef]
2. Frazer, G.J.; Williams, C.G.; Abramovich, Y.I.; San-Antonio, G. A Regular Two-Dimensional over-Sampled Sparse Receiving Array for Over-The-Horizon Radar. In Proceedings of the 2015 IEEE Radar Conference (RadarCon), Arlington, VA, USA, 10–15 May 2015; pp. 840–845.
3. San Antonio, G.; Abramovich, Y.I. Two-Dimensional High Frequency Surface Wave Radar Receive Array Design. In Proceedings of the 2017 IEEE Radar Conference (Radarconf), Seattle, WA, USA, 8–12 May 2017; pp. 1402–1407.
4. Gaytan, D.; Hilton, D.; Buchanan, K.; Xu, L.; Dinh, V.; Larson, G.; Dilay, C. HF Noise Trends in Coastal Southern California. In Proceedings of the 2017 IEEE International Symposium on Antennas and Propagation & USNC/URSI National Radio Science Meeting, San Diego, CA, USA, 9–14 July 2017; pp. 207–208.

5. Xiaolin, Q.; Ming, J.; Xinpeng, M. Atmospheric Noise Suppression for HF Radar. In Proceedings of the 2001 CIE International Conference on Radar Proceedings (Cat No.01TH8559), Beijing, China, 15–18 October 2001; pp. 992–995.
6. Giesbrecht, J.; Clarke, R.; Abbott, D. An empirical study of the probability density function of hf noise. *Fluct. Noise Lett.* **2006**, *6*, L117–L125. [CrossRef]
7. Coleman, C.J. A Direction-Sensitive Model of Atmospheric Noise and Its Application to the Analysis of HF Receiving Antennas: A direction-sensitive model of atmospheric noise. *Radio Sci.* **2002**, *37*, 1–10. [CrossRef]
8. Pederick, L.H.; Cervera, M.A. A Directional HF Noise Model: Calibration and Validation in the Australian Region: Directional HF Noise Model. *Radio Sci.* **2016**, *51*, 25–39. [CrossRef]
9. Witvliet, B.A.; Alsina-Pagès, R.M.; Altadill, D.; van Maanen, E.; Laanstra, G.J. Separation of Ambient Radio Noise and Radio Signals Received via Ionospheric Propagation. *Atmosphere* **2023**, *14*, 529. [CrossRef]
10. Keller, C.M. HF Noise Environment Models. *Radio Sci.* **1991**, *26*, 981–995. [CrossRef]
11. Hagn, G.H.; Stehle, R.H.; Harnish, L.O. Shortwave Broadcasting Band Spectrum Occupancy and Signal Levels in the Continental United States and Western Europe. *IEEE Trans. Broadcast.* **1988**, *34*, 115–125. [CrossRef]
12. Watterson, C.; Juroshek, J.; Bensema, W. Experimental Confirmation of an HF Channel Model. *IEEE Trans. Commun. Technol.* **1970**, *18*, 792–803. [CrossRef]
13. Ghosh, B.B.; Mitra, S.N. Measurement of Atmospheric Noise. *IETE J. Res.* **1958**, *5*, 2–16. [CrossRef]
14. Ibukun, O. Structural Aspects of Atmospheric Radio Noise in the Tropics. *Proc. IEEE* **1966**, *54*, 361–367. [CrossRef]
15. Lemmon, J.J. Wideband Model of HF Atmospheric Radio Noise. *Radio Sci.* **2001**, *36*, 1385–1391. [CrossRef]
16. International Telecommunication Union (ITU). *Radio Noise*; ITU-R Rep. P.372-16; ITU: Geneva, Switzerland, 2022.
17. International Telecommunication Union (ITU). *Ground Wave Propagation Prediction Method for Frequencies between 10 KHz and 30 MHz*; ITU-R Rep P.368-10; ITU: Geneva, Switzerland, 2022.
18. Kotaki, M. Global Distribution of Atmospheric Radio Noise Derived from Thunderstorm Activity. *J. Atmos. Terr. Phys.* **1984**, *46*, 867–877. [CrossRef]
19. Gibson, A.J.; Arnett, L. Azimuthal Distribution of Noise and Interface at HF. In Proceedings of the 1993 Eighth International Conference on Antennas and Propagation, Edinburgh, UK, 30 March–2 April 1993; Volume 1, pp. 356–359.
20. Cecil, D.J.; Buechler, D.E.; Blakeslee, R.J. Gridded Lightning Climatology from TRMM-LIS and OTD: Dataset Description. *Atmos. Res.* **2014**, *135–136*, 404–414. [CrossRef]
21. Christian, H.J. Global Frequency and Distribution of Lightning as Observed from Space by the Optical Transient Detector. *J. Geophys. Res.* **2003**, *108*, 4005. [CrossRef]
22. Fockens, K.T.W.H.; Leferink, F. Correlation Between Measured Man-Made Noise Levels and the Density of Habitation. *IEEE Trans. Electromagn. Compat.* **2020**, *62*, 2696–2703. [CrossRef]
23. Ivanov, N.V.; Kopytenko, Y.A.; Tereshchenko, E.D.; Tereshchenko, P.E. Features of Resonance Structures in Natural Electromagnetic Noise Spectra in the Region of the Main Ionospheric Trough. *Geomagn. Aeron.* **2017**, *57*, 752–760. [CrossRef]
24. Zhang, X.; Yang, Q.; Yao, D.; Deng, W. Main-Lobe Cancellation of the Space Spread Clutter for Target Detection in HFSWR. *IEEE J. Sel. Top. Signal Process.* **2015**, *9*, 1632–1638. [CrossRef]
25. Li, G.; Lu, Q.; Lao, G.; Ye, W. Wideband Noise Interference Suppression for Sparsity-Based SAR Imaging Based on Dechirping and Double Subspace Extraction. *Electronics* **2019**, *8*, 1019. [CrossRef]
26. Yang, X.; Zhang, Z.; Zeng, T.; Long, T.; Sarkar, T.K. Mainlobe Interference Suppression Based on Eigen-Projection Processing and Covariance Matrix Reconstruction. *IEEE Antennas Wirel. Propag. Lett.* **2014**, *13*, 1369–1372. [CrossRef]
27. Guo, X.; Sun, H.; Yeo, T.S. Interference Cancellation for High-Frequency Surface Wave Radar. *IEEE Trans. Geosci. Remote Sens.* **2008**, *46*, 1879–1891. [CrossRef]
28. Yao, D.; Deng, W.; Zhang, X.; Yang, Q.; Zhang, J.; Li, J. Main-lobe Clutter Suppression Algorithm Based on Rotating Beam Method and Optimal Sample Selection for Small-aperture HFSWR. *IET Radar Sonar Navig.* **2019**, *13*, 1162–1170. [CrossRef]
29. Xue, W.; Luo, Y.; Yang, Y.; Huang, Y. Noise Suppression for GPR Data Based on SVD of Window-Length-Optimized Hankel Matrix. *Sensors* **2019**, *19*, 3807. [CrossRef] [PubMed]
30. Guo, Y.; Wei, Y.; Xu, R.; Yu, L. New BSS-based ABF for Heterogeneous Ionospheric Clutter Mitigation in HFSWR. *IET Radar Sonar Navig.* **2019**, *13*, 2015–2023. [CrossRef]
31. Anbiyaei, M.R.; Liu, W.; McLernon, D.C. White Noise Reduction for Wideband Linear Array Signal Processing. *IET Signal Process.* **2018**, *12*, 335–345. [CrossRef]
32. Xiong, J.; Pan, J.; Du, M. A Cascade Network for Pattern Recognition Based on Radar Signal Characteristics in Noisy Environments. *Remote Sens.* **2023**, *15*, 4083. [CrossRef]
33. Ghosh, J.; Vargas-Rosales, C.; Mendes, L.L.; Ra, I.-H.; Nhan Vo, V.; Aimtongkham, P.; So-In, C. A Novel Transceiver and an Asynchronous Mode for the Hybrid Multiple-Access HetNet Architecture. *IEEE Access* **2023**, *11*, 135609–135625. [CrossRef]
34. Li, T.; Zhang, Z. Analysis and Design of HF Radio Noise Measurement Antennas Considering Directivity and Polarization. In Proceedings of the 2019 IEEE 9th International Conference on Electronics Information and Emergency Communication (ICEIEC), Beijing, China, 12–14 July 2019; pp. 483–486.
35. Sangmahamad, P.; Janpugdee, P.; Zhao, Y. A Metasurface-Based Electronically Reconfigurable and Dual-Polarized Reflectarray Antenna for Beam-Steering Applications. *IEEE Access* **2023**, *11*, 137414–137425. [CrossRef]

36. Xu, Y.; Liu, G.; Jiang, T. Leveraging Rough-Relay-Surface Scattering for Non-Line-of-Sight mmWave Radar Sensing. *IEEE Internet Things J.* **2023**. [CrossRef]
37. Yao, D.; Chen, Q.; Tian, Q. Space-Time Cascaded Processing-Based Adaptive Transient Interference Mitigation for Compact HFSWR. *Remote Sens.* **2023**, *15*, 651. [CrossRef]
38. Chen, S.; Lin, Y.; Yuan, Y.; Li, J.; Wang, X.; Zhu, L.; Zhang, S. Airborne SAR Suppression of Blanket Jamming Based on Second Order Blind Identification and Fractional Order Fourier Transform. *IEEE Trans. Geosci. Remote Sens.* **2023**, *61*, 5212014. [CrossRef]
39. Wang, Y.; Mao, X.; Zhang, J.; Ji, Y. Detection of Vessel Targets in Sea Clutter Using In Situ Sea State Measurements With HFSWR. *IEEE Geosci. Remote Sens. Lett.* **2018**, *15*, 302–306. [CrossRef]
40. Sun, W.; Li, X.; Pang, Z.; Ji, Y.; Dai, Y.; Huang, W. Track-to-Track Association Based on Maximum Likelihood Estimation for T/R-R Composite Compact HFSWR. *IEEE Trans. Geosci. Remote Sens.* **2023**, *61*, 5102012. [CrossRef]
41. Zhang, J.; Zhang, X.; Deng, W.; Guo, L.; Yang, Q. A Novel Main-Lobe Cancellation Method Based on a Single Notch Space Filter and Optimized Correlation Analysis Strategy. *Int. J. Antennas Propag.* **2019**, *2019*, 1495097. [CrossRef]
42. Zhang, J.; Deng, W.; Zhang, X.; Yang, Q. Improved Main-Lobe Cancellation Method for Space Spread Clutter Suppression in HFSSWR. In Proceedings of the 2018 IEEE Radar Conference (RadarConf18), Oklahoma City, OK, USA, 23–27 April 2018; pp. 197–201.
43. Guo, L.; Deng, W.; Yao, D.; Yang, Q.; Ye, L.; Zhang, X. A Knowledge-Based Auxiliary Channel STAP for Target Detection in Shipborne HFSWR. *Remote Sens.* **2021**, *13*, 621. [CrossRef]
44. Buckley, K.; Griffiths, L. An Adaptive Generalized Sidelobe Canceller with Derivative Constraints. *IEEE Trans. Antennas Propag.* **1986**, *34*, 311–319. [CrossRef]
45. Guo, M.; Jensen, S.H.; Jensen, J. Novel Acoustic Feedback Cancellation Approaches in Hearing Aid Applications Using Probe Noise and Probe Noise Enhancement. *IEEE Trans. Audio Speech Lang. Process.* **2012**, *20*, 2549–2563. [CrossRef]